HHS Public Access

Author manuscript

Adv Funct Mater. Author manuscript; available in PMC 2024 August 15.

Published in final edited form as:

Adv Funct Mater. 2023 August 15; 33(33): . doi:10.1002/adfm.202301839.

Simulation of Cortical and Cancellous Bone to Accelerate Tissue Regeneration

Zhihai Fan[a], **Hongxiang Liu**[a], **Zhaozhao Ding**[b,c], **Liying Xiao**[b,c], **Qiang Lu**[b], **David L Kaplan**[d]

[a]Department of Orthopedics, The Second Affiliated Hospital of Soochow University, Suzhou 215000, People's Republic of China

[b]State Key Laboratory of Radiation Medicine and Radiation Protection, Institutes for Translational Medicine, Soochow University, Suzhou 215123, People's Republic of China

[c]National Engineering Laboratory for Modern Silk & Collaborative Innovation Center of Suzhou Nano Science and Technology, Soochow University, Suzhou 215123, People's Republic of China

[d]Department of Biomedical Engineering, Tufts University, Medford, Massachusetts 02155, United States

Abstract

Different tissues have complex anisotropic structures to support biological functions. Mimicking these complex structures *in vitro* remains a challenge in biomaterials designs in support of tissue regeneration. Here, inspired by different types of silk nanofibers, a composite materials strategy was pursued towards this challenge. A combination of fabrication methods was utilized to achieve separate control of amorphous and beta-sheet rich silk nanofibers in the same solution. Aqueous solutions containing these two structural types of silk nanofibers were then simultaneously treated with an electric field and with ethylene glycol diglycidyl ether (EGDE). Under these conditions, the beta-sheet rich silk nanofibers in the mixture responded to the electric field while the amorphous nanofibers were active in the crosslinking process with the EGDE. As a result, cryogels with anisotropic structures were prepared, including mimics for cortical- and cancellous-like bone biomaterials as a complex osteoinductive niche. *In vitro* studies revealed that mechanical cues of the cryogels induced osteodifferentiation of stem cells while the anisotropy inside the cryogels influenced immune reactions of macrophages. These bioactive cryogels also stimulated improved bone regeneration *in vivo* through modulation of inflammation, angiogenesis and osteogenesis responses, suggesting an effective strategy to develop bioactive matrices with complex anisotropic structures beneficial to tissue regeneration.

Graphical Abstract

The cryogels composed of amorphous silk nanofibers and beta-sheet rich silk nanofibers were fabricated to achieve spatio-simulation of cortical and cancellous bone. The spatio-anisotropic features of different regions favored quicker bone regeneration through tuning osteogenic and

Corresponding author: Qiang Lu, Tel: (+86)-512-67061649; Lvqiang78@suda.edu.cn.

Supporting Information

The Supporting Information is available free of charge.

inflammatory behaviors effectively. The novel fabricating strategy realized the design of bioactive matrices with complex special anisotropy to improve tissue regeneration outcomes.

Keywords

anistropic; osteoinductivity; immunomodulation; bone regeneration; silk nanofiber

Introduction

Bone defects often cause severe pain and disability, requiring medical intervention with autografts, allografts or artificial grafts.[1–3] Artificial bone grafts avoid the shortcomings of natural bone-derived grafts such as donor site injury and limited donor material.[3,4] However, a gap remains for artificial grafts in terms of osteoconductivity, osteoinductivity and osseoingegration, fostering continuing research into bioactive bone grafts with ECM-biomimetic features.

In-depth understanding of the bone healing process addresses the function of cytokines and bioactive molecules secreted from cells.[5, 6] Different growth factors and bioactive ingredients were loaded in the grafts and released into the repair site through diffusion or degradation.[7–9] Although the released molecules accelerated bone regeneration through immuno-regulation and angiogenic/osteogenic stimulation,[7,8,10] the release behavior usually mismatchs with healing stages, resulting in reduced bone regeneration outcomes. Cells sense the physiological microenvironment and then secrete cytokines responsively to maintain biological functions.[10–13] Mimicking the bone extracellular matrix (ECM) is considered an effective option to develop matrices with improved osteogenic and angiogenic capacities. The key features include micro-and nano-scale hierarchical structures, anisotropic topographies, mechanical properties and porosity. All the features influence cell proliferation, migration, aggregation and secretion, and then impact bone regeneration.[12–17] Different physical and mechanical features show synergistic action to control immunological reactions, angiogenesis and osteogenesisfor in this bone healing process, suggesting advantages of bone grafts with appropriate biomimetic features.[10–12, 16–18] Natural lamellar bone is composed of dense cortical bone and spongy cancellous bone. The cortical bone has an anisotropic lamellar structure to provide high mechanical strength, while the cancellous bone is composed of a homogeneous porous structure that facilitates bone metabolism and hematopoietic functions.[14, 19] Bone matrices with hierarchical microstructures, mechanical properties and gradient cues were developed to mimic native bone ECM. Although the matrices achived faster bone healing and better functional recovery,[17, 20–22] the simultaneous mimicking of both cortical and cancellous bone within single scaffold remains a technical challenge. Different methods such as modular assembly and liquid-phase co-synthesis were used to prepare scaffolds with different structures for osteochondral and nerve tissue engineering.[23–25] However, mimicking different regions without a hard interface between the regions remains a problem, hindering optimal repair of bone tissue.

Silk fibroin is a candidate polymer to design bioactive bone grafts with different biomimetic physical cues.[7, 8, 26–29] Tough porous silk scaffolds were developed to provide biophysical and biomechanical cues in bone regeneration.[8, 27] Silk nanofibers were also assembled in aqueous solution and used to build bone matrices with a biomimetic microenvironment.[28] Porous silk nanofiber-based cryogel scaffolds and tough silk nanofiber hydrogels with anisotropic structures were separately prepared to mimic cortical and cancellous bone, respectively, and exhibited anticipated osteogenic capacity.[16, 29] However, fabricating both of these physical features in a single scaffold was not achieved. In the present study, the goal was to achieve multiple regions within a single silk-based scaffold to mimic bone cortical and cancellous regions. A blend solution composed of amorphous silk nanofibers (ASNFs) and beta-sheet rich silk nanofibers (BSNFs) was treated with an annular electrical field and an ethylene glycol diglycidyl ether (EGDE) crosslinking system, simultaneously (Scheme 1). The BSNFs selectively migrated to the periphery under the annular electrical field to form lamellar structures (cortical bone-like), while the ASNFs that were inert to the electrical field were selectively crosslinked with EGDE to form a homogeneous porous structure (cancellous bone-like). Different mechanical properties were also achieved in this process to provide biomechanical cues in the different regions. *In vitro* studies revealed that the different regions in the cryogel scaffolds exhibited anticipated anti-inflammatory, angiogenic and osteogenic capacity. Significantly improved anti-inflammation and osteogenesis were observed in the composite cryogels, suggesting cooperative action of different physical cues. The fastest bone healing with the highest quality were also achieved when the rats were treated with the cryogels containing these mixed hierarchical structures and regions.

2. Material and methods

2.1 Preparation of BSNF hydrogel:

Anhydrous Na_2CO_3 (59.36 g) and silk (70 g) were added to deionized water (28 L) to degum the raw silk. [7] After being boiled for 30 min, the degummed silk was scrubbed and dried for further use. Then, the degummed silk was mixed with 9.3 mol/L lithium bromide solution in a 27:100 wt/wt and dissolved in an oven at 60°C for 4 h.[8] After dialysis in deionized water to remove the lithium bromide for 3 days, the solution was centrifuged twice (4°C, 9,000 rpm, 20 min) to remove impurities, obtaining aqueous silk fibroin solutions with a concentration of about 6 wt%. The silk fibroin in the aqueous solution was self-assembled into metastable 100 nm particles after slow concentrating to above 20% for about 72 h at 60°C. The concentrated solution was diluted to 2 wt% with distilled water and incubated hermetically in an oven at 60°C until the formation of BSNF hydrogels.

2.2 Preparation of ASNF solution

The degummed silk (2 g) was added to the mixed solution of formic acid (80%, 4.14 mL) and lithium bromide solution (8 mol/L, 95.86 mL), sealed in an oven at 60°C for 6 h to dissolve the silk.[16] The solution was dialyzed in deionized water to remove the lithium bromide and formic acid for 3 days at 4°C. Then the solution was centrifuged twice (4°C,

9,000 rpm, 15 min) to obtain the ASNFs. The ASNF solution was concentrated to about 11 % at 60°C and stored at 4°C for further use.

2.3 Preparation of cryogels with hierarchical structures

The crosslinking agent ethylene glycol diglycidyl ether (EGDE), the catalyst tetramethylethylenediamine (TEMED), and ASNF solution (11 wt%) were mixed 10:1:400 (vol/vol/vol).[29] Then, the BSNF hydrogel (2 wt%) was introduced to the mixed solution at a volume ratio of 3:1, 2:1, 1:1, 1:2 and 1:3 (BSNF: ASNF) at room temperature with a magnetic stirrer. The mixed solutions were poured into an annular graphite tank with the outer graphite ring connected to the positive electrode and the inner graphite column connected to the negative electrode. After treatment in an electrical field (50 V DC) for 1 min, the BSNF migrated near the annular graphite tank and gelled again. The system containing both gel and solution was placed in a refrigerator at −20°C for 24 h to induce the crosslinking of ASNF. After thawing at room temperature, the cryogels had two parts without a solid interface, where the peripheral region was composed of dense anisotropic porous structure (SNFH-A) while the interior region exhibited a homogeneous porous structure (SNFH-H). The whole cryogel was termed SNFH-AH.

2.4 Characterization of the cryogels

The micromorphology of different cryogels was investigated with scanning electron microscopy (SEM, S-4800, Hitachi, Tokyo, Japan). The samples were lyophilized for 2 days and cut into thick slices (1 mm). Before observation, the samples were sputter-coated with gold (10 mA, 90 s).[30] Based on the SEM images, the structure and pore size of the samples were analyzed using Image J software. The lyophilized samples were ground and then pressed into thin slices to analyze secondary structure through Fourier transform infrared spectroscopy (FTIR, Nicolet 5700, Thermo Scientific, FL, America). The wave number range was 400 to 4000 cm^{-1}.

2.5 Porosity Measurements

The cryogels' porosity was measured according to the method reported previously.[31] The mass of freeze-dried cryogels were named as m_1. After being immersed in boiled distilled water for 2 h, the bubbles were expelled from the cryogels and the water fills the pores. The mass of the hydrated samples were recorded as m_2. The porosity was calculated by the formula as follows:

$$P\,(\%) = (m_2 - m_1)/\rho V \times 100\%$$

Here, P represented the porosity of the samples, ρ represented the density of distilled water, V represented the volume of the samples. Three samples in aach group were measured.

2.6 Mechanical properties

The mechanical properties of all samples were tested via food texture analyzers (TMS-Pro, FTC, USA). The inner and outer parts of the cryogels were cut with hole punch and separated at the boundary along the longitudinal axis of the tube. Three cryogels for each

group were soaked in ultrapure water for 24 h. Every part (5 mm in edge length and 10 mm in height) was compressed parallel to and perpendicular to the anisotropy direction. The parameters were set to a compression rate of 2 mm/min and a deformation rate of 60% of the original height.[8]

2.7 Degradation

The degradation of different cryogels was evaluated via enzyme degradation *in vitro*. All cryogels (30 mg) were immersed in protease XIV solutions (5 U/mL) and maintained in an oscillating water bath at 37°C.[32] The protease solutions were replaced every 4 days. At the designed time points, the cryogels were washed with distilled water and dried at 60°C for more than 24 h. Three replicate measurements were performed for each time point. The samples were also immersed in phosphate-buffered saline solution (PBS) as a control. The degradation rate was calculated as follows:

$$\varepsilon(\%) = (m_a - m_b)/m_a \times 100\%$$

where ε expressed the degradation rate of the cryogel, m_a represented the initial mass of the cryogel, and m_b is the mass of the remaining cryogel after degradation.

2.8 *In vitro* cytocompatibility of cryogels

Bone mesenchymal stem cells (BMSCs) were extracted from 3-week-old male Sprague-Dawley (SD) rats (40 g). The use of experimental animals was approved by the animal ethics committee of Soochow University and was carried out in accordance with the Soochow University's guidelines for the care and use of laboratory animals (202103A113, Mar, 2021). BMSCs were cultured in modified Eagle medium (DMEM, low glucose) supplemented with 10% fetal bovine serum (FBS) and 100 U/mL penicillin-streptomycin (both from Invitrogen, Carlsbad, CA) in a cell culture incubator at 37°C with 5% CO_2. BMSCs were seeded in each cryogel with a length of 5 mm and height of 2 mm at a cell density of 1×10^5 after the cryogels were sterilized with ^{60}Co γ-irradiation at the dose of 25 kGY.[8] Samples were removed after days 1, 3, and 7 of incubation, washed with PBS, and lyophilized for 72 h. All samples were digested overnight with proteinase K. DNA was extracted from the cryogels using the Tissue DNA kit (Invitrogen, Carlsbad, CA, USA), and detected via the PicoGreen DNA assay (Invitrogen, Carlsbad, CA, USA).[33] The fluorescence intensity of each sample was monitored using a BioTeK Synergy 4 spectrofluorometer (BioTeK, Winooski, VT, USA) with an excitation wavelength of 480 nm and an emission wavelength of 530 nm. The DNA content of each group was calculated from the standard curve. In addition, the cytocompatibility of cryogels was also evaluated by confocal laser scanning microscopy (CLSM, Olympus FV10 inverted microscope, Nagano, Japan). When the cells were cultured on the cryogels for 1, 3, and 7 days, the samples were rinsed three times with PBS and fixed with 4% paraformaldehyde (PFA) for 0.5 h. The samples were rinsed three times with PBS again and permeabilized with 0.1% (v/v) TritonX-100 (Sigma, St Louis, USA) for 10 min. The F-actin was stained with tetramethylrhodamine (TRITC)-phalloidin (Thermo Fisher, Waltham, MA, USA) for 60 min, and the nucleus was stained with 4',6-diamidino-2-phenylindole (DAPI) for 10 min in dark at room temperature. The number, morphology and distribution of cells in the cryogels were observed with CLSM (Olympus FV10 inverted

microscope, Nagano, Japan). The orientation of cell aggregates and the orientation angle of nuclei were also determined by Image J software.

2.9 Cell osteodifferentiation *in vitro*

The BMSCs (5×10^4 cells per well) were seeded in the cryogels and cultured with osteogenic differentiation medium (89% low glucose-DMEM, 10% FBS, 0.05 mM ascorbic acid-2-phosphate, 1% streptomycin-penicillin, 10 nM dexamethasone, and 10 mM sodium-β-glycerophosphate) for 7, 14, and 21 days, respectively. At the corresponding time points, the cell-seeded cryogels were lyophilized for 48 h before proteins were extracted from the cryogels using RIPA lysis buffer. Total proteins were quantified with BCA assay (Thermo Scientific, Waltham, MA, USA).[34] The cell lysates were tested with an alkaline phosphatase (ALP) activity assay kit (Biovision, San Francisco, USA) to assess ALP activity. The protein solution was mixed with p-nitrophenol phosphate substrate (pNPP, 5mM) and incubated at 20°C for 1 h in the dark before the NaOH solution was added to terminate the reaction.[8] P-nitrophenol (pNP) was used as the substrate, and the released free p-nitrophenol molecules were calculated by reading the absorbance intensity using a microplate reader (Bio-Rad Laboratories, Philadelphia, PA, USA) at 405 nm. ALP activity was normalized according to the total protein content above.

Alizarin Red S (ARS) powder was dissolved in ultra-pure water with a concentration of 20 mg/mL. The pH was adjusted to 4.2 with dilute hydrochloric acid.[35] The cryogels were rinsed with PBS and fixed with 4% PFA at room temperature for 15 min. The calcium nodules in the cryogels were stained with the ARS dye at room temperature for 30 min. Then the free dye was washed off with ultrapure water. The calcium nodules were stained purple-red or black-purple and observed by microscopy.

mRNA expression level of osteogenesis-related genes including runt-related transcription factor 2 (RUNX2) and osteopontin (OPN) were detected with quantitative real-time polymerase chain reaction (qRT-PCR). Trizol (Invitrogen, Carlsbad, CA, USA) was used to extract total cellular RNA. After the RNA was purified with a RNeasy Mini Kit (Applied Biosystems, Carlsbad, CA, USA), the concentration of the extracted RNA was detected with Nano Drop 2000 (Thermo Scientific, Waltham, MA). Total RNA was reverse transcribed into complementary DNA (cDNA) with a high-capacity cDNA reverse transcription kit (Applied Biosystems, Carlsbad, CA) and a 2720 thermal cycler (Applied Biosystems, Foster City, CA, USA). Real-Time PCR results were obtained through a 7500 real-time PCR system (Applied Biosystems, Foster City, CA, USA) and fast SYBR green kit (Applied Biosystems, Carlsbad, CA, USA). The reaction conditions were as follows: 95°C (5 min), 95°C (10 s) for 40 cycles, and 60°C (1 min). The internal control gene was glyceraldehyde-3-phosphate dehydrogenase (GAPDH), and the primer sequences are listed in Table 1. Target gene expression was calculated according to the $2^{-\Delta\Delta Ct}$ formula with reference to the respective controls.

2.10 *In vitro* macrophage-polarization

RAW 264.7 cells (2×10^4 cells/well, obtained from the Cell Bank of the Chinese Academy of Sciences, Shanghai, China) were seeded on the cryogels and cell slides respectively to

evaluate macrophage polarization. Macrophages were cultured in DMEM (high glucose) supplemented with 10% FBS, and 100 U/mL penicillin−streptomycin. At day 7, total RNA macrophages was extracted from different groups based on the method mentioned above and macrophage polarization was assessed by expression of inducible nitric oxide synthase (iNOS) and CD 206. The primer sequences are listed in Table 1.

The proteins produced by macrophages were also extracted and detected to analyze the expression of iNOS and CD 206 by Western Blot. Protein buffer was added to the cellular proteins and heated in a boiling water bath to denature the proteins. Additional samples were also analyzed by sodium dodecyl sulfate-polyacrylamide gel electrophoresis (SDS-PAGE) and transferred to a polyvinylidene difluoride membrane. After blocking the membranes with 5% skim milk, the membranes were incubated at 4°C with primary antibodies as follows: 1:1000, Anti-iNOS antibody (ab178945, Abcam, Cambridge, MA, USA); 1:1000, Anti-CD206 antibody (ab64693, Abcam, Cambridge, MA, USA). The GAPDH monoclonal antibody (1:500, RLM3029, RuiYingBio, China) was also used as an internal control. Blots were incubated with secondary antibodies at room temperature for 1 h and visualized with a chemiluminescence reagent kit. The expression of iNOS and CD 206 from the Western Blot images were analyzed via Image J software. When macrophages were cultured for 3 and 7 days, the concentration of cytokines secreted by M_1 and M_2 macrophages (IL-6, IL-10 and BMP-2) into the culture medium were detected by ELISA. The samples were measured with a BioTeK Synergy 4 spectrofluorometer. The concentrations of different cytokines were calculated according to the standard curves.

2.11 Effect of macrophage polarization on osteodifferentiation

Macrophages and BMSCs were co-cultured in Transwell chambers. Macrophages were seeded onto the different materials at a cell density of 5×10^4 and placed in the upper chamber of Transwells, while BMSCs were seeded on the cell slides at a cell density of 1×10^4 in the lower chamber of the Transwell. After 24 hrs culture in complete medium (89% high glucose DMEM, 10% FBS, 1% double antibodies), the seeded cells were cultured in osteogenic differentiation medium (10 nmol/L dexamethasone, 0.05 mmol/L ascorbic acid-2-phosphate, and 10 mmol/L sodium-β-glycerophosphate) for 7 days. ARS and qRT-PCR were used to evaluate the osteodifferentiation of BMSCs. BMSCs were fixed with 4% PFA for 15 min at room temperature and the expression of ALP was detected using an alkaline phosphatase color development kit following the manufacturer's instructions. Immunofluorescence was also used to evaluate the expression of RUNX2. After fixation for 30 min with PFA, the BMSCs were permeabilized with 0.1% TritonX-100 permeabilization solution for 10 min and then with 3% bovine serum albumin (BSA) solution for 1 h. The primary antibody (Anti-RUNX2 antibody) was diluted with 1% BSA, and the cells were incubated in a StainTray slide staining system at room temperature with the primary antibody dilutions for 3–5 h in dark. Then BMSCs were incubated with the secondary antibody solutions that were diluted with 3% BSA solutions. The cytoskeleton and nucleus of the cells were stained with etramethylrhodamine (TRITC)-phalloidin and DAPI, respectively, and observed with a CLSM (Olympus FV10 inverted microscope, Nagano, Japan).

2.12 The construction of rat femoral condyle defect model

A rat femoral defect model was established to evaluate the performance of the bionic cryogels in promoting bone tissue regeneration *in vivo*.[8] Thirty-two 8-week-old male Sprague-Dawley (SD) rats weighing 250–300 g were purchased from the animal resource center of Soochow University. All procedures and operations were approved by the animal ethics committee of Soochow University (202106A0563, June 2021). The rats were divided into 4 groups at random: blank, SNFH-A, SNFH-H, SNFH-AH. After anesthesia with 3% pentobarbital sodium at a dose of 0.1 mL/100 g, the rats were shaved and drilled to form the defect with a diameter of 3 mm on the bilateral distal femur. The defects were filled with the different cryogels (height: 5mm; diameter: 3 mm). Finally, the wounds in the rats were sutured and housed in pathogen free (SPF) laboratory animal rooms. At 2, 4, 8, and 12 weeks, the rats were sacrificed through an intraperitoneal injection of 3% pentobarbital sodium. The bone specimens were collected for further analysis.

2.13 Microcomputed tomography (Micro-CT) of specimens

After fixing with 10% buffered neutralized formalin for 48 h, all bone specimens were scanned by a Bruker Micro-CT Skyscan 1276 system (Kontich, Belgium). A software CT Analyser (version 1.18.8.0) was used to analyze the 2D and 3D images of the bone micro architectures in a region of interest (ROI). Scan settings were as follows: medium resolution, voxel size 10 μm, 85 kV, 200 mA, Al filter 1 mm and integration time 384 ms.

2.14 Histological staining of the specimens *in vivo*:

At the desired time points, the specimens were decalcified with 10% EDTA (Ethylene Diamine Tetraacetic Acid) for 4 weeks at pH 7.4 after scanning by Micro-CT. The decalcified specimens were dehydrated with gradient alcohol solutions and embedded in paraffin. After sectioning, the samples were stained with hematoxylin eosin (HE), Masson's trichrome, immunofluorescence targeting CD68 (Abcam, ab283654), CD206 (Abcam, ab64693), iNOS (Abcam, ab178945), CD31 (Abcam, ab64543), α-smooth muscle actin (α-SMA, Abcam, ab240678), COL-1 (Abcam, ab6308) and immunohistochemistry targeting OPN (Abcam, ab214050) to evaluate tissue ingrowth, immunomodulation, vascularization and new bone formation at the defect sites. A goldner stain was used to evaluate the mineralized bone and non-mineralized bone.[36] Those stained images were also analyzed quantitatively with Image J.

2.15 Statistical analysis

The mean±standard deviation were utilized to present all quantitative information. All results were evaluated by one-way or two-way analysis of variance (ANOVA) followed by Sidak's multiple comparison test (*P < 0.05, **P <0.01, and ***P < 0.001). *P < 0.05 was considered statistical difference.

Results and Discussion

Formation and characterization of hydrogels with hierarchical structures

BSNFs were previously used to design ECM-biomimetic scaffolds.[8,16,37] The silk nanofibers have a negative surface charge with zeta potential value of −31.4±2.5 mV, endowing migration capacity in an electrical field.[34] Silk nanofiber hydrogels with aligned structures were also fabricated to control the migration, proliferation and differentiation of stem cells, accelerating tissue regeneration.[8, 34, 38] Compared to traditional silk fibroin in aqueous solution, the tyrosine amide acids migrated into the inside of the silk nanofibers (BSNF).[39] Thus, significantly fewer phenyl hydroxyl groups distributed on the surface and crosslinkers can't move to the inside area of the nanofibers, which makes the nanofibers relatively inert to HRP and EGDE crosslinking systems.[16, 29] To enrich the silk nanofiber family, the ASNFs were prepared using a lithium bromide-formic acid solvent.[29] Unlike BSNFs, ASNFs have significantly fewer negative charges with the zeta potential value of about −7.6±0.52 mV, but display a richer phenyl hydroxyl group on the surface, making them active in various crosslinking systems,[16, 29, 40] but inert in electrical fields. The different responses of BSNFs and ASNFs to electric field and EGDE crosslinking inspired us to design a combined fabrication system to mimic the complex ECM of bone. The two silk nanofibers were blended in the same aqueous solution and treated both with an electrical field and EGDE crosslinkers.

To mimic the annular lamellar and porous structures of cortical bone and cancellous bone, respectively, the annular electrical field was used to control the migration of BSNFs to structurally mimic cortical regions, while the EGDE crosslinker induced the ASNFs to form porous structures similar to the cancellous region. Silk fibroin-based cryogels with good bio-safety and biocompatibility have been prepared through crosslinker EGDE and catalyst TEMED in several studies.[29, 41–43] In the crosslinking reaction, the phenyl hydroxyl group was reacted to crosslink various silk fibroins, inducing cryogel formation.[29, 41–43] Since the ASNFs had richer phenyl group on the nanofiber surface, the cryogels with higher crosslinking density were prepared and achieved significant higher mechanical properties than that prepared with traditional silk fibroin soluiton under same crosslinking conditions.[29, 43] The tough ASNF cryogels had suitable stiffness to induce osteodifferentiation and were used to form homogeneous porous scaffolds in our present study. As shown in Scheme 1, when the blended solutions were treated with the electrical field and EGDE simultaneously, the BSNFs migrated toward the positive electrode and assembled to annular lamellar hydrogels while the ASNFs remained stationary and were gradually crosslinked through EGDE. Since the BSNFs were inert to the EGDE crosslinking, the freezing-thawing process had no influence on the anisotropic nanofiber hydrogel regions that had formed. Thus, the complex cryogels with different regions were prepared after freezing-thaw treatment (Fig. 1 a–c). The silk nanofibers could form networks in aqueous solution to restrain the directional growth of ice in freezing process.[29, 43] The cancellous bone-like region was composed of homogeneous porous cryogels with a high porosity above 87.5% and pore sizes about 147.9±16.3 μm (Fig. 1 a, e, f). The cortical bone-like region were consisted of BSNFs and ASNFs while the cancellous bone-like regions were mainly composed of ASNFs, suggesting higher silk fibroin concentration in the cortical bone-like

region. Denser structures with smaller pore size existed in the cortical bone-like region wherein the assembled BSNFs in the electrical field resulted in the anisotropic lamellar porous structure with lamellar interval of about 67.3±18.2 μm (Fig. 1 a, d). Since the original ASNFs distributed homogeneously in the blend solution and remained stationary in the electrical field, the cryogels formed from amorphous nanofibers became a continuous phase to connect the anisotropic lamellar region and homogeneous porous region, avoiding a hard interface (Fig. 1 a). Higher magnification images of the pore walls in the two different regions revealed that the lamellar walls were composed of aligned nanofibers along the long axis, while random nanofibers distributed homogeneously in the porous walls, similar to cortical bone and cancellous bone at the micron level (Fig. 1 a). Thus, the hierarchical mimicking of cortical and cancellous regions without a hard interface was achieved through this relatively simple fabrication system.[24, 44] The shape of the cryogels could be regulated through the electrical field and the shape of the electrodes, such as tubes, plates and semi-circles (Fig. 1 j–l). Our previous studies revealed that the BSNFs migrated gradually under electrical fields to form anisotropic silk nanofiber hydrogels near the positive electrode.[16, 34, 45] The thickness of anisotropic hydrogels was controlled through changing the treatment time under electrical field. The ratio of amorphous and beta-sheet rich silk nanofibers in the beginning solution could also influence the thickness of different parts. Thus, the thickness of cortical and cancellous bones was controllable through tuning the fabricating conditions to mimic the different parts of bone tissues.

Amorphous silk nanofibers transformed to beta-sheet structures after freezing-thaw, to improve the mechanical properties.[29] Similar to pure cryogels derived from ASNFs, the two regions of the hydrogels had similar beta-sheet structures, which endowed the cryogels with water-stability and tough mechanical performance (Fig. 1 g, Fig. S1). Based on our recent study, the concentration of ASNFs was about 10%, which could provide an optimal porous structure and osteogenic mechanical cues.[29] Due to the maxinum concentration of BSNF in aqueous solution was 2 wt%, the introduction of BSNF to ASNF solution (11 wt%) resulted in the concentration decrease of ASNF in the blend solution. If the volume ratios of BSNF (2wt%) and ASNF (11 wt%) were 3:1 and 2:1, the tough cryogels failed to form due to the low concentration of ASNF (about 2.7–3.7%) in the blend solutions (Fig. S1). The cryogels could be preprared when the volume ratios of BSNF and ASNF was below 1:1 where the best mechanical properties were achieved when the ratio of BSNF and ASNF was 1:2 (Fig. S1). The mechanical properties of the anisotropic regions were influenced by both aligned BSNFs and homogeneous crosslinked ASNFs. The highest anisotropic mechanical difference was appeared in the cryogels derived from the blend solution containing 1wt% BSNF and 5.5 wt% ASNF (the volume ratio of BSNF and ASNF, 1:1), but the anisotropic mechanical property at different regions degraded if the cryogels were prepared with the blend solution containing 0.5 wt% BSNF and 8.2 wt% ASNF (the volume ratio of BSNF and ASNF, 1:3). Considering the mechanical properties and anisotropic performances, the BSNF (2 wt%) and ASNF (11 wt%) solutions were blended at volume ratio of 1:2 and used to prepare the cortical- and cancellous-like cryogels. Figure. 1h shows the compressive stress and modulus of the different regions of the cryogels when the samples were compressed parallel to and orthogonal to the aligned nanofibers in the cortical like regions. The inner region with homogeneous porous structures showed similar mechanical properties at

different orientations. The moduli were 369.4±21.8 kPa and 354.2±25.3 kPa, respectively, similar to cryogels prepared with pure amorphous silk nanofiber solutions at the same concentration.[29] The results confirmed that the BSNFs had no negative influence on the crosslinking of the amorphous nanofibers in the blend solutions. The BSNFs as anisotropic reinforced fibers have been used to prepare tough silk-based hydrogels.[16] The BSNFs also improved the mechanical properties of the peripheral regions in the present systems. Compared to that of the inner area (cancellous bone-like regions), the modulus increased to 581±14.2 kPa at the peripheral area when the samples were compressed orthogonal to the oriented beta-sheet rich nanofibers. The aligned structures in the peripheral regions resulted in anisotropic mechanical properties where the modulus was 616±19.4 kPa when the samples were compressed parallel to the aligned nanofibers. Although the mechanical performance was inferior to natural cortical and cancellous bones,[46] the two regions provided sufficient osteogenic mechanical cues to induce the osteodifferentiation of stem cells.[16, 29] The different microstructures of the two regions resulted in different degradation behavior (Fig. 1 i). Due to the beta-sheet rich structures of the hydrogels, the two regions remained stable in PBS solution, maintaining >90% of original weight after 28 days. The introduction of aligned silk nanofibers improved the stability of the peripheral region. When cultured in protease XIV solution (5 U/ml) for 28 days, the degradation ratios of the peripheral and inner regions were 40% and 45%, respectively. The slow degradation of the porous tough cryogels could provide longer-term support for the regenerated tissues. Thus, the complex silk nanofiber cryogels showed microstructures, mechanical properties and degradation behavior comparable to cortical and cancellous bones.

In vitro cell behavior in cryogels

Compared to matrices prepared with traditional silk fibroin,[47–49] silk nanofiber-based scaffolds and hydrogels exhibit improved cytocompatibility due to the ECM-like nanostructures.[8, 16, 29] Although the different parts of the composite cryogels were composed of silk nanofibers with similar rich beta-sheet content, the various porous structures led to discrepant cell behavior. The center region with homogeneous porous structures was similar to our reported macroporous silk nanofiber cryogels.[29] At the same amorphous silk nanofiber concentration, the cryogels were also prepared from pure amorphous silk nanofiber solutions without the exposure to the electric field (ASNF-H) and these materials were compared with the inner region of the composite cryogels. BMSCs seeded on the two cryogels showed similar proliferation and osteodifferentiation behavior, confirming similar cytocompatibility. Thus, the inner region with homogeneous porous structures were used as a control in the *in vitro* study. The composite cryogels were divided into three parts (peripheral region with aligned porous structure, the inner region with homogeneous porous structure, and the middle region with both of the porous structures) and seeded with BMSCs to evaluate cytocompatibility. The three regions with different porous structures were termed SNFH-A, SNFH-H and SNFH-AH. At day 1, the cells distributed and adhered well in both the homogeneous and anisotropic porous areas without aggregation (Fig. 2a). The seeded cells then exhibited continuous proliferation inside the different cryogels and occupied most of porous areas at day 7, suggesting cytocompatibility (Fig. 2a). DNA content confirmed sustained cell proliferation in the different cryogels (Fig. 2e). Previous studies revealed that larger pores facilitated cell migration and proliferation,

resulting in improved cytocompatibility.[17, 48, 50] Compared to the inner homogeneous porous region, the cells in the peripheral region with smaller pores showed slower proliferation while the cells in the middle region with both homogeneous and anisotropic pores exhibited intermediate proliferation behavior (Fig. 2e). The results indicated that the composite cryogels maintained good cytocompatibility and tuned cell proliferation through the porous structures. The different topographies in the different regions also influenced cell migration and aggregation (Fig. 2 a–c). As expected, when cultured in the cryogels with anisotropic and homogeneous porous structures, cells formed circular oriented aggregates and homogeneous aggregates, respectively. When the cells were cultured in the cryogels with both porous structures, the cells maintained homogeneous aggregates in the areas with different porous structures.

Mechanical cues are a critical determinant in inducing osteogenic differentiation of BMSCs.[16, 51, 52] Our previous study revealed that the cryogels with a stiffness above 31.6 kPa induced the osteodifferentiation of BMSCs.[29] Higher stiffness usually implies stronger mechanical cues to induce osteogenic behaviors.[16, 29, 43] Thus, the osteogenic capacity of the cryogels was improved following the increase in stiffness. When BMSCs were cultured in the cryogels with different porous structures and stiffness for 14 and 28 days, the highest osteodifferentiation was achieved for the cells in the SNFH-A cryogel with the highest modulus, while the cells in the SNFH-H cryogel with the lowest stiffness showed the weakest osteodifferentiation (Fig. 2 d, f, g). The SNFH-AH cryogel composed of both soft and hard regions showed intermediate osteogenic capacity. The ARS (Alizarin Red S) stained results implied that mechanical cues had a decisive effect on osteogenic capacity in these porous cryogels (Fig. 2 d). The expression of different osteogenic genes and enzymes, such as ALP, RUNX-2 and OPN, suggested the same osteogenic tendency in the different cryogels where the highest expression of the genes and enzymes occurred in the cells cultured in the SNFH-A cryogels (Fig. 2 f, g).

Immune modulation is an effective strategy to optimize angiogenesis and osteogenesis in bone healing.[10–12, 53] Immunomodulating biomaterials have been fabricated by controlling microstructure, topography and compositions of the matrices or loading suitable cytokines and drugs to induce immune cells,[10–14, 53] which then recruited endogenous stem cells and regulated angiogenic and osteogenic behavior at different stages of bone regeneration. Since anisotropic topography is considered an inducing factor for M_2 polarization,[53] macrophages were also seeded on the different cryogels. Using the cell slide as a control, all the silk nanofiber cryogels resulted in significantly higher expression of CD 206 (M_2) and lower expression of iNOS (M_1) by the macrophages (Fig. 3 a–d). The results suggested that silk nanofiber cryogels had anti-inflammation effect, consistent with previous studies.[54–57] The various topographies of the silk nanofiber cryogels induced diverse polarization of macrophages. Compared to that in the SNFH-H cryogels, a higher ratio of M_2/M_1 macrophages appeared in the SNFH-A cryogels with anisotropic structures (Fig. 3d). Thus, similar to other immunomodulating biomaterials,[11, 13] the aligned topography in silk nanofiber cryogels stimulated the anti-inflammation phenotype of macrophages, beneficial to bone regeneration. Although the SNFH-AH cryogels had both homogeneous porous structures (relative lower M_2 polarization) and anisotropic porous structures (relative higher M_2 polarization), the highest ratio outcome of M_2/M_1 was achieved, superior to

that of the pure SNFH-A and SNFH-H. The Western blot results confirmed the best M_2 polarization of macrophages in the SNFH-AH cryogels (Fig. 3 c, d). These results suggested that the coexistence of anisotropic and homogeneous porous structures provided a synergistic effect on the macrophages, resulting in better M_2 polarization than the cryogels with the single porous structure. The higher ratio of M_2 macrophages is conductive to an anti-inflammatory microenvironment. As expected, significantly higher amounts of anti-inflammatory cytokine (IL-10) and lower amount of inflammatory cytokine (IL-6) were secreted from the macrophages cultured in the SNFH-AH and SNFH-A cryogels, where the best anti-inflammatory niche existed in the SNFH-AH cryogel system (Fig. 3 e, f). Further studies are necessary to clarify the specific function of different cues such as morphogical and mechanical factors in immune regulation. It is anticipated to achieve better anti-inflammatory capacity through introducing other bioactive ingredients such as curcumin to the cryogel system, which would be realized in our future study. The anti-inflammatory microenvironments facilitated osteogenesis. The secretion of BMP-2 from the macrophages seeded in various cryogels was also investigated and showed the highest amount in the SNFH-AH cryogel group (Fig. 3 g). To further reveal the influence of immunomodulation on osteogenic differentiation in these cryogels, both BMSCs and macrophages were co-cultured in different hydrogels for 7 days to induce the osteodifferentiation (Fig. 4 a–e). BMSCs and macrophages were also co-cultured on the cell slides as a control. Compared with single BMSCs cultured on the cell slides, the co-culture of BMSCs and macrophages never stimulated more osteodifferentiation of BMSCs due to the inferior anti-inflammation modulation by the sheet. All the BMSCs co-cultured with macrophages in the different silk nanofiber cryogels showed higher osteodifferentiation, indicating the stimulating effect from the macrophages. Due to better mechanical osteogenic cues and anti-inflammation performance of the silk nanofiber cryogels with anisotropic structures, the osteodifferentiation of BMSCs in the SNFH-A cryogels was significantly better than that in the SNFH-H cryogels. Although pure BMSCs cultured in the SNFH-A cryogels were easier to differentiate into osteoblasts than that in the SNFH-AH cryogels due to the mechanical cues, the best osteodifferentiation appeared in the SNFH-AH cryogel group in the co-culture system. Therefore, through modulating immune behavior and mechanical factors simultaneously, the cryogels containing both anisotropic and homogeneous porous structures created a well-orchestrated microenvironment for osteogenesis.

In vivo bone regeneration treated with cryogels

To evaluate the function of the cryogels on bone regeneration *in vivo*, a rat femur defect model was developed and treated with the different cryogels. The immunomodulation of the cryogels at the defect site *in vivo* was evaluated after 2 weeks post-implantation (Fig. 5 a, b, d). In the blank control, the macrophages at the defect site were mainly composed of M_1 phenotype (Fig. 3 a). Little M_2 phenotype appeared at the bone defects, indicating that bone regeneration was at the inflammation stage. Similar to the *in vitro* results, the ratio of M_2 gradually increased in the defects when treated with the SNFH-H, SNFH-A and SNFH-AH cryogels, respectively (Fig. 3 b). Almost all of the macrophages maintained the M_2 phenotype at the defects filled with the SNFH-AH cryogels, suggesting the most beneficial niche for bone healing. Therefore, the aligned and homogeneous porous structures optimized anti-inflammatory microenvironments at the defect sites to stimulate bone regeneration.

Previous studies revealed that immunomodulation at the defect sites was also critical for rapid angiogenesis.[18, 58–60] When the cryogels were implanted for 2 weeks, the sections collected from the defects were stained with CD31 and α-SMA to visualize blood vessels (Fig. 5 c, e). As expected, the various silk nanofiber cryogels stimulated angiogenesis at the bone defect sites where the defects treated with the cryogels with higher anti-inflammation capacity showed better angiogenesis. The highest amount of blood vessels appeared in the SNFH-AH cryogel group, which would favor the ingrowth of bone tissues. Consistent with the *in vivo* anti-inflammatory and angiogenesis behaviors, the healing rates gradually increased when the defects were filled with the SNFH-H, SNFH-A and SNFH-AH cryogels, respectively (Fig. 6 a). After 12 weeks, above 72% of defect areas had been occupied by the new bone tissue in the SNFH-AH group while only about 40% of the defect was filled with bone tissue in the blank group. The quantitative analysis of micro-CT images further confirmed the best osteoinductive capacity by the SNFH-AH cryogels. After 12 weeks, the values of Tb.Sp were 0.59±0.04, 0.75±0.03, and 0.48±0.03 while Tb.Th was 0.51±0.02, 0.43±0.02, and 0.63±0.03 for the defects treated with the SNFH-A, SNFH-H and SNFH-AH cryogels, respectively (Fig. 6 b, c). A similar tendency was observed for bone mineral density and trabecular thickness, where the highest mineral density and trabecular thickness was achieved in the SNFH-AH group (Fig. 6 d, e). All of the results confirmed that the SNFH-AH cryogels induced the fastest healing rate with the best quality of bone based on mineral density.

The HE staining images exhibited various bone regeneration processes in these groups (Fig. 7 a, Fig. S2). All the porous cryogels facilitated ingrowth of granulation tissues. At week 2, most of the defect areas were filled by granulation tissue in the different cryogel groups while significant unfilled areas existed at the defect site in the blank group. After 4 weeks, the defects in the blank group were filled with fibrotic tissue without new bone formation. Significant new bone tissues were regenerated in all the cryogel groups where the highest amount was achieved in the SNFH-AH cryogel group. The best osteogenesis was maintained when the defects were treated with the SNFH-AH cryogel for 8 and 12 weeks, confirming its osteogenic capacity *in vivo*. To further evaluate the quality of the new bone formed, the defect sections were collected after 12 weeks post-implantation and stained with Masson's trichrome (Fig. 7 b). The confocal images of Masson's trichrome-stained defects confirmed the best bone regeneration in the SNFH-AH cryogel group, surpassing the SNFH-H and SNFH-A cryogel groups. Most of defects were occupied by new bone tissue and a significantly higher ratio of mature bone existed in the defects treated with the SNFH-AH cryogels. The immunofluorescence staining of OPN was also performed to evaluate the quality of the regenerated bone tissues (Fig. 7 c). Similar to other staining results, the highest ratio of mature bone tissues was achieved in the SNFH-AH cryogel group, confirming the best quality of the new bone tissue. Thus, the silk cryogels with hierarchical mimics of cortical and cancellous bones provided a well-orchestrated niche to modulate inflammation, angiogenesis and osteogenesis to accelerate bone healing. The defects treated with the SNFH-AH cryogels were also stained to evaluate the local influence of the anisotropic porous region and homogeneous porous region on bone regeneration (Fig. 8). At week 2, some new blood vessels appeared at the anisotropic outer region while little angiogenesis was found in the homogeneous region. The results suggested that new

blood vessels first formed at the outer region, similar to normal bone regeneration processes. After 8 weeks, significantly more blood vessels appeared in the homogeneous inner region, which also suggested similar vascularization to normal cortical and cancellous bones. The BSNFs as carries have been used to load both hydrophilic and hydrophobic molecules such as deferoxamine, nerve growth factor and curcumin.[8, 28, 29, 61] It is possible to load angiogenic molecules on the BSNFs to prepare the drug-laden cortical and cancellous-like scaffolds. The loaded molecules could be immobilized in the cortical regions to control the angiogenesis kinetically through tuning the density and release behavior of the angiogenic molecules, which will be realized in our following study. Twelve weeks after surgery, although the exact ratios of components were different than normal bone tissues, and significantly higher collagen deposited in the inner region, the regenerated bone tissues in the anisotropic porous regions showed a higher ratio of mineralized bone, while more non-mineralized bone tissues existed in the amorphous porous regions, which had similar composition to normal bone tissues (Fig. 8 b, c).[62] The results imply that the silk cryogels with hierarchical simulating structures induce better recovery of damaged bones. The ratios of the cortical and cancellous-like regions could be regulated through tuning the ratio of BSNF and ASNF and the treating time under electric field. It is possible to optimize the ratio of the two regions in future to improve the osteogenic capacity in various bone tissues.

Conclusions

Cryogels with hierarchical structures were prepared by tuning the mixture of two types of nanofibers in aqueous solution. The beta sheet rich silk nanofibers migrated to the peripheral regions to form anisotropic lamellar structures while amorphous silk nanofibers crosslinked in the interior to induce homogeneous porous structures, simulating hierarchical microstructures of cortical and cancellous bones simultaneously. Both *in vitro* and *in vivo* results revealed that these hierarchical biomimetic structures actively modulated inflammation, angiogenesis and osteogenesis, superior to cryogels with ECM-like structures of either cortical or cancellous bone. The quickest bone regeneration with the best healing quality was achieved with the cryogels with the dual regions of hierarchical structures, offering promising utility for bone tissue engineering and regeneration. The combination of different fabrication methods and various responses to the silk nanofibers suggests the design of bioactive matrices with complex special anisotropy to improve tissue regeneration outcomes.

Supplementary Material

Refer to Web version on PubMed Central for supplementary material.

Acknowledgements

Both Zhihai Fan and Hongxiang Liu contributed equally to the work. The authors thank the National Nature Science Foundation of China (52273143) and the NIH (R01NS094218, R01AR070975). We also thank the Project of State Key Laboratory of Radiation Medicine and Protection, Soochow University (GZK1202119), Gusu Health Talents Program (GSWS2021021) and Suzhou Key Project of Clinical Diagnosis and Treatment Technologies for Key Diseases (LCZX202205) for support of this work.

References

[1]. Chen CY, Chen CC, Wang CY, Lee AKX, Yeh CL, Lin CP, Polymers 2020, 12, 1455. [PubMed: 32610580]

[2]. Li JJ, Ebied M, Xu J, Zreiqat H, Adv. Healthcare Mater 2018, 7, e1701061.

[3]. Rodríguez-Merchán EC, Int. J. Mol. Sci 2022, 23, 7430. [PubMed: 35806435]

[4]. Ho-Shui-Ling A, Bolander J, Rustom LE, Johnson AW, Luyten FP, Picart C, Biomaterials 2018, 180, 143. [PubMed: 30036727]

[5]. Sordi MB, Cruz A, Fredel MC, Magini R, Sharpe PT, Mater. Sci. Eng. C. Mater. Biol. Appl 2021, 124, 112055. [PubMed: 33947549]

[6]. Ziegler CG, van Sloun R, Gonzalez S, Whitney KE, DePhillipo NN, Kennedy MI, Dornan GJ, Evans TA, Huard J, LaPrade RF, Am. J. Sports Med 2019, 47, 2174. [PubMed: 31034242]

[7]. Ding ZZ, Fan ZH, Huang XW, Bai SM, Song DW, Lu Q, Kaplan DL, J. Mater. Chem. B 2016, 4, 3555. [PubMed: 27482381]

[8]. Fan Z, Liu H, Shi S, Ding Z, Zhang Z, Lu Q, Kaplan DL, Mater. Today Bio 2022, 15, 100283.

[9]. Boda SK, Almoshari Y, Wang H, Wang X, Reinhardt RA, Duan B, Wang D, Xie J, Acta Biomater 2019, 85, 282. [PubMed: 30605770]

[10]. Wang Y, Wang J, Gao R, Liu X, Feng Z, Zhang C, Huang P, Dong A, Kong D, Wang W, Biomaterials 2022, 285, 121538. [PubMed: 35504180]

[11]. Zhu Y, Liang H, Liu X, Wu J, Yang C, Wong TM, Kwan KYH, Cheung KMC, Wu S, Yeung KWK, Sci. Adv 2021, 7, eabf6654.

[12]. Wang J, Meng F, Song W, Jin J, Ma Q, Fei D, Fang L, Chen L, Wang Q, Zhang Y, Int. J. Nanomedicine 2018, 13, 4029. [PubMed: 30022825]

[13]. Dong X, Liu S, Yang Y, Gao S, Li W, Cao J, Wan Y, Huang Z, Fan G, Chen Q, Wang H, Zhu M, Kong D, Biomaterials 2021, 272, 120767. [PubMed: 33813259]

[14]. Zhu L, Luo D, Liu Y, Int. J. Oral. Sci 2020, 12, 6. [PubMed: 32024822]

[15]. Anderson HJ, Sahoo JK, Wells J, van Nuffel S, Dhowre HS, Oreffo ROC, Zelzer M, Ulijn RV, Dalby MJ, Sci. Rep 2022, 12, 8165. [PubMed: 35581256]

[16]. Xu G, Ding Z, Lu Q, Zhang X, Zhou X, Xiao L, Lu G, Kaplan DL, Protein Cell 2020, 11, 267. [PubMed: 32048173]

[17]. Diloksumpan P, Bolaños RV, Cokelaere S, Pouran B, de Grauw J, van Rijen M, van Weeren R, Levato R, Malda J, Adv. Healthcare Mater 2020, 9, e1901807.

[18]. Shi M, Xia L, Chen Z, Lv F, Zhu H, Wei F, Han S, Chang J, Xiao Y, Wu C, Biomaterials 2017, 144, 176. [PubMed: 28837959]

[19]. Wubneh A, Tsekoura EK, Ayranci C, Uludağ H, Acta Biomater 2018, 80, 1. [PubMed: 30248515]

[20]. Karamat-Ullah N, Demidov Y, Schramm M, Grumme D, Auer J, Bohr C, Brachvogel B, Maleki H, ACS Biomater. Sci. Eng 2021, 7, 4545. [PubMed: 34415718]

[21]. Xu N, Ye X, Wei D, Zhong J, Chen Y, Xu G, He D, ACS Appl. Mater. Interfaces 2014, 6, 14952. [PubMed: 25133309]

[22]. Guo Y, Tran RT, Xie D, Wang Y, Nguyen DY, Gerhard E, Guo J, Tang J, Zhang Z, Bai X, Yang J, J. Biomed. Mater. Res. A 2015, 103, 772. [PubMed: 24829094]

[23]. Fu JN, Wang X, Yang M, Chen YR, Zhang JY, Deng RH, Zhang ZN, Yu JK, Yuan FZ, Front. Bioeng. Biotechnol 2021, 9, 812383. [PubMed: 35087809]

[24]. Li JJ, Kim K, Roohani-Esfahani SI, Guo J, Kaplan DL, Zreiqat H, J. Mater Chem. B 2015, 3, 5361. [PubMed: 26167284]

[25]. Chang YC, Chen MH, Liao SY, Wu HC, Kuan CH, Sun JS, Wang TW, ACS Appl. Mater. Interfaces 2017, 9, 37623. [PubMed: 28990762]

[26]. Zhao ZH, Ma XL, Zhao B, Tian P, Ma JX, Kang JY, Zhang Y, Guo Y, Sun L, Cell prolif 2021, 54, e13043. [PubMed: 34008897]

[27]. Chen Z, Zhang Q, Li H, Wei Q, Zhao X, Chen F, Bioact. Mater 2021, 6, 589. [PubMed: 33005824]

[28]. Cheng W, Ding Z, Zheng X, Lu Q, Kong X, Zhou X, Lu G, Kaplan DL, Biomater. Sci 2020, 8, 2537. [PubMed: 32215404]

[29]. Zhang X, Hang Y, Ding Z, Xiao L, Cheng W, Lu Q, Biomacromolecules 2022, 23, 2160. [PubMed: 35443774]

[30]. Zhang ZS, Ding ZZ, Huang JW, Qin JZ, Shen YX, Zhang F, Zuo BQ, Int. J. Biol. Macromol 2018, 117, 144. [PubMed: 29803750]

[31]. Mohammadi H, Sepantafar M, Muhamad N, Bakar Sulong A, Adv. Eng. Mater 2021, 23, 2100463.

[32]. Han H, Ning H, Liu S, Lu Q, Fan Z, Lu H, Lu G, Kaplan DL, Adv. Funct. Mater 2016, 26, 421. [PubMed: 27293388]

[33]. Han F, Liu S, Liu X, Pei Y, Bai S, Zhao H, Lu Q, Ma F, Kaplan DL, Zhu H, Acta Biomater 2014, 10, 921. [PubMed: 24090985]

[34]. Lu Q, Zhang F, Cheng W, Gao X, Ding Z, Zhang X, Lu Q, Kaplan DL, Adv. Healthcare Mater 2021, 10, e2100427.

[35]. Kim J, Kim HD, Park J, Lee E, Kim E, Lee SS, Yang J-K, Lee Y-S, Hwang NS, Biomater. Res 2018, 22, 1. [PubMed: 29308274]

[36]. Stoetzel S, Malhan D, Wild U, Helbing C, Hassan F, Attia S, Jandt KD, Heiss C, El Khassawna T, Int. J. Mol. Sci 2021, 23, 374. [PubMed: 35008800]

[37]. Zhang X, Xiao L, Ding Z, Lu Q, Kaplan DL, ACS Nano 2022, 16, 10209 [PubMed: 35587205]

[38]. Lu G, Ding Z, Wei Y, Lu X, Lu Q, Kaplan DL, ACS Appl. Mater. Interfaces 2018, 10, 44314. [PubMed: 30507148]

[39]. Ling S, Li C, Jin K, Kaplan DL, Buehler MJ, Adv. Mater 2016, 28, 7783. [PubMed: 27352291]

[40]. Dong X, Zhao Q, Xiao L, Lu Q, Kaplan DL, Biomacromolecules 2016, 17, 3000. [PubMed: 27476755]

[41]. Mao Z, Bi X, Ye F, Shu X, Sun L, Guan J, Ritchie RO, Wu S, ACS Biomater. Sci. Eng 2020, 6, 4512. [PubMed: 33455190]

[42]. Yetiskin B, Okay O, Int. J. Biol. Macromol 2019, 122, 1279. [PubMed: 30227202]

[43]. Hou J, Ding Z, Zheng X, Shen Y, Lu Q, Kaplan DL, Adv. Healthcare Mater 2023, 25, e2203050.

[44]. Wang XF, Fang J, Zhu WW, Zhong CX, Ye DD, Zhu MY, Lu X, Zhao YS, Ren FZ, Adv. Funct. Mater 2021, 31, 2010068.

[45]. Lu Q, Bai S, Ding Z, Guo H, Shao Z, Zhu H, Kaplan DL, Adv. Mater. Interfaces 2016, 3, 1500687.

[46]. Li Z, Du T, Ruan C, Niu X, Bioact. Mater 2021, 6, 1491. [PubMed: 33294729]

[47]. Collins MN, Ren G, Young K, Pina S, Reis RL, Oliveira JM, Adv. Funct. Mater 2021, 31, 2010609.

[48]. Zou S, Wang X, Fan S, Yao X, Zhang Y, Shao H, J. Mater. Chem. B 2021, 9, 5514. [PubMed: 34152355]

[49]. Wang K, Xu M, Zhu M, Su H, Wang H, Kong D, Wang L, J. Biomed. Mater. Res. A 2013, 101, 3474. [PubMed: 23606405]

[50]. Lai J, Wang C, Liu J, Chen S, Liu C, Huang X, Wu J, Pan Y, Xie Y, Wang M, Biofabrication 2022, 14, 45006.

[51]. Hu Q, Liu M, Chen G, Xu Z, Lv Y, ACS Appl. Mater. Interfaces 2018, 10, 27669. [PubMed: 30063134]

[52]. Liu Y, Yang G, Ji H, Xiang T, Luo E, Zhou S, Colloids Surf. B. Biointerfaces 2017, 154, 1. [PubMed: 28268191]

[53]. Tan S, Wang Y, Du Y, Xiao Y, Zhang S, Bioact. Mater 2021, 6, 3411. [PubMed: 33842737]

[54]. Dong X, Zhao SX, Yin XL, Wang HY, Wei Z-G, Zhang YQ, Int. J. Biol. Macromol 2020, 150, 1061. [PubMed: 31743716]

[55]. Zhou F, Zhang X, Cai D, Li J, Mu Q, Zhang W, Zhu S, Jiang Y, Shen W, Zhang S, Ouyang HW, Acta Biomater 2017, 63, 64. [PubMed: 28890259]

[56]. Ma Y, Duan L, Sun J, Gou S, Chen F, Liang Y, Dai F, Xiao B, Biomaterials 2022, 282, 121410. [PubMed: 35202934]

[57]. Nadri S, Rahmani A, Hosseini SH, Habibizadeh M, Araghi M, Mostafavi H, Artif. Cell Nanomed. B 2022, 50, 40.

[58]. Zheng ZW, Chen YH, Wu DY, Wang JB, Lv MM, Wang XS, Sun J, Zhang ZY, Theranostics 2018, 8, 5482. [PubMed: 30555559]

[59]. Yin C, Zhao Q, Li W, Zhao Z, Wang J, Deng T, Zhang P, Shen K, Li Z, Zhang Y, Acta Biomater 2020, 102, 416. [PubMed: 31760223]

[60]. Lee J, Byun H, Madhurakkat Perikamana SK, Lee S, Shin H, Adv. Healthcare Mater 2019, 8, e1801106.

[61]. Gao X, Cheng W, Zhang X, Zhou Z, Ding Z, Zhou X, Lu Q, Kaplan DL, ACS Appl. Mater. Interfaces 2022, 14, 3701. [PubMed: 35006667]

[62]. Fonseca H, Moreira-Gonçalves D, Coriolano HJ, Duarte JA, Sports Med 2014, 44, 37. [PubMed: 24092631]

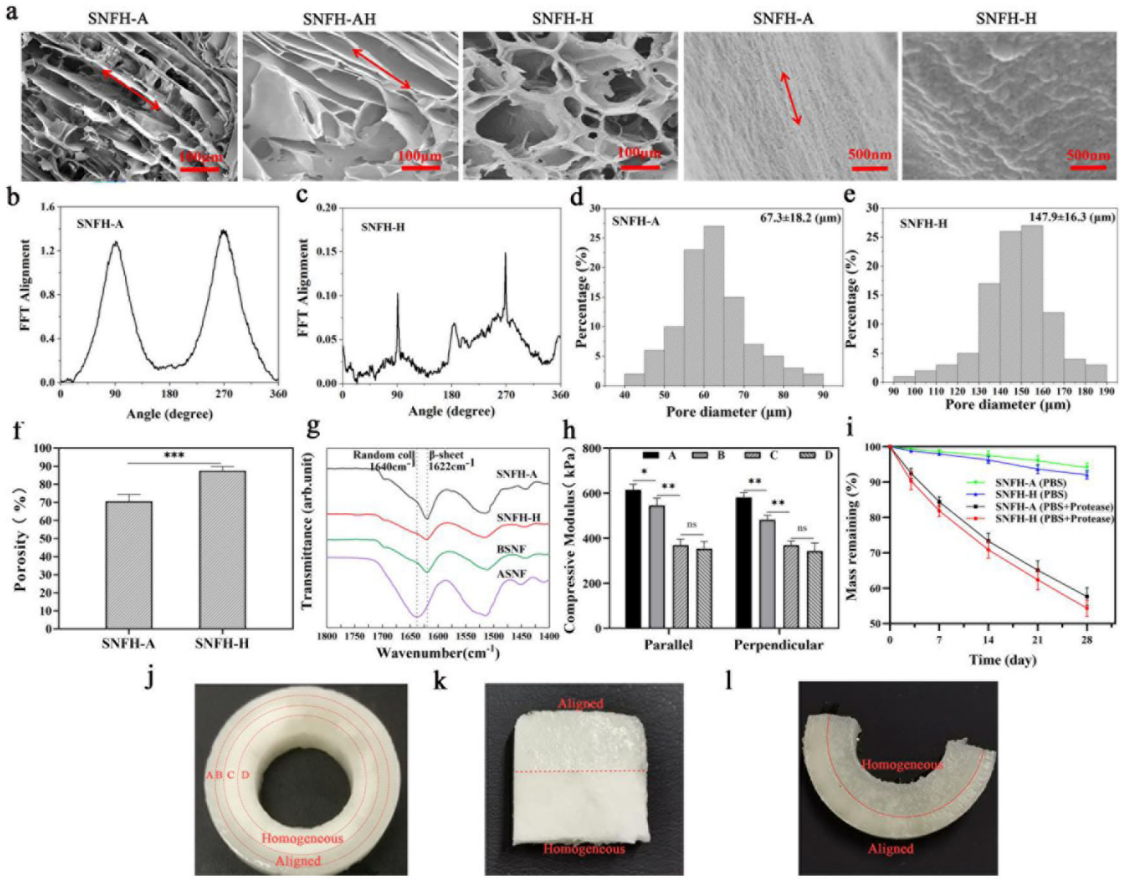

Figure. 1.

Characterization of cryogels: (a) SEM images with different magnifications of the cryogels. (b, c) Degree of alignment. (d, e) Pore sizes. (f) Porosities. (g) FTIR spectra. (h) Compressive modulus. (i) The degradation behavior in PBS and protease XIV solutions. (j, k, l) Various shapes of the composite cryogels with hierarchical structures, such as tube, plate and semi-circle. Red dot lines is the interface of aligned regions and homogeneous regions. Red arrows represents the direction of aligned SNF. The samples listed as: SNFH-A, the peripheral region of the cryogels composed of silk nanofibers with aligned porous structures; SNFH-H, the inner region of the cryogels composed of silk nanofibers with homogeneous porous structures; SNFH-AH, the middle region of the cryogels composed of silk nanofibers with both of the porous structures; A, B, C, and D in picture h represent the different regions of the composite cryogels from peripheral to inner regions, respectively. The different regions (A, B, C, D) listed in the cryogel image (j). Data presented as mean ± SD, n=3, the error bars indicate the SD, p-values calculated using one-way ANOVA with Sidak's multiple comparison tests, *$p < 0.05$, **$p < 0.01$, and ***$p < 0.001$. NS means no statistical difference ($P > 0.05$).

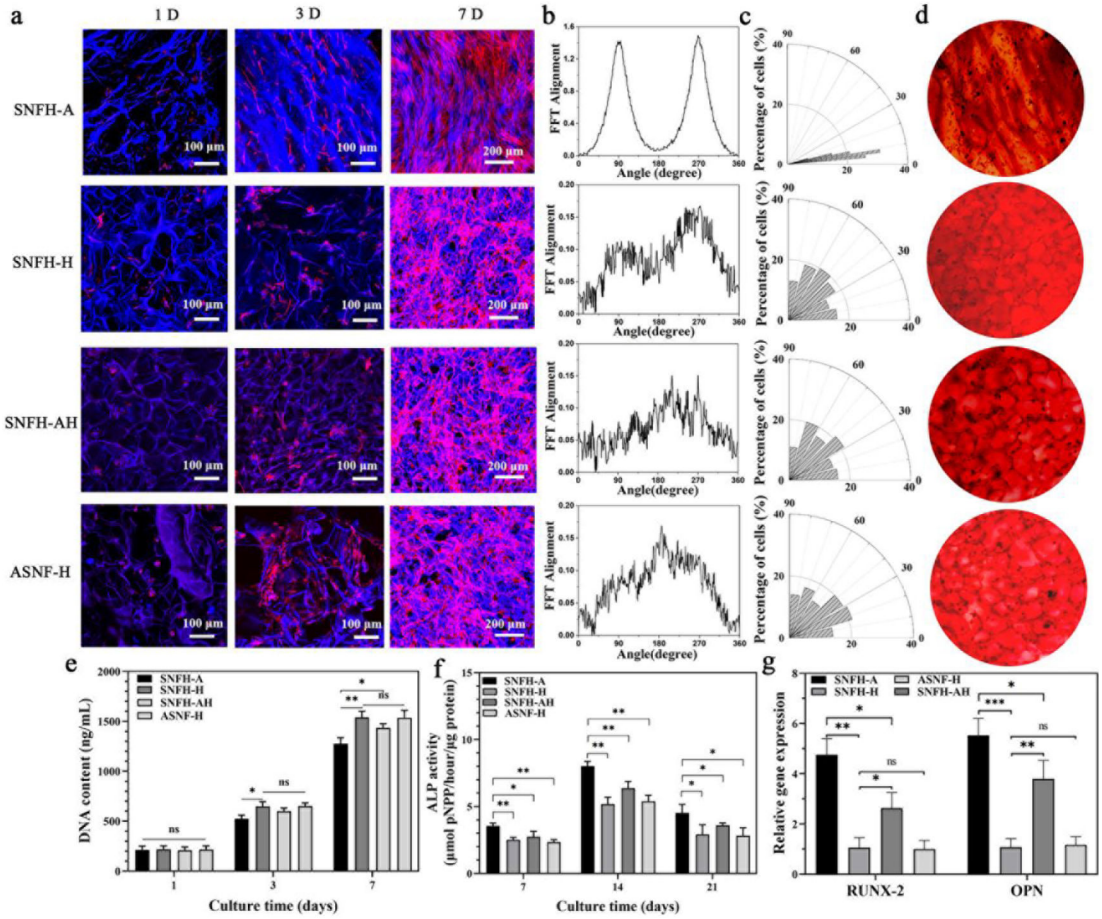

Figure 2.

In vitro proliferation and osteodifferentiation of BMSCs on the different cryogels: (a) Confocal microscopy images of BMSCs cultured on the different cryogels for 1, 3 and 7 days. (b) Degree of alignment and (c) alignment angles of BMSCs. The alignment degree and angles were analyzed by Image J software according to the CLSM images. The alignment degree means the orientation of cytoskeletons' directions between cells, while the alignment angle is the angle between the long axis of the nucleus and the aligned direction of materials. Both the FFT peaks and narrow alignment angle distribution indicated good aligned distribution. (d) ARS staining of BMSCs. (e) Proliferation of BMSCs on day 1, 3 and 7. (f) Alkaline phosphatase activity, (g) mRNA levels of RUNX-2-related transcription factor and osteopontin (OPN) of BMSCs. ASNF-H represents the homogeneous porous cryogels which were prepared from the pure amorphous silk nanofiber solution without electrical field treatment. Data presented as mean ± SD, n=3, the error bars indicate the SD, p-values calculated using one-way ANOVA with Sidak's multiple comparison tests, *$p < 0.05$, **$p < 0.01$, and ***$p < 0.001$. NS means no statistical difference ($P > 0.05$).

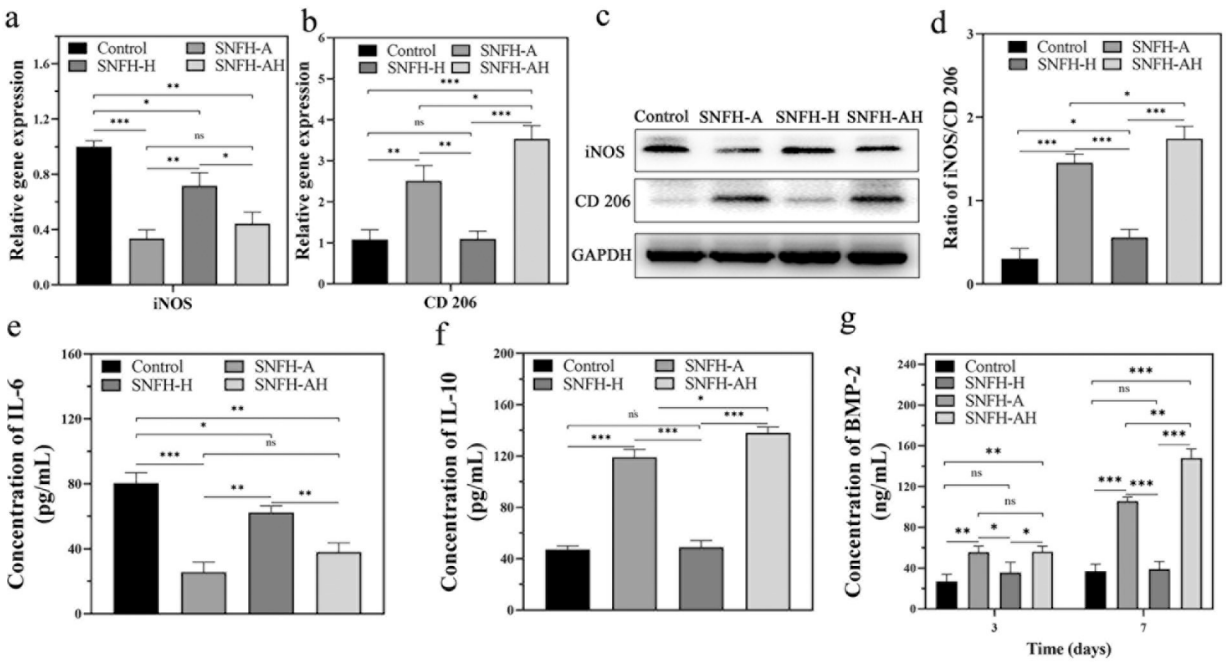

Figure 3.

In vitro polarization behavior of macrophages on the different cryogels: (a, b) The mRNA levels of iNOS (M_1) and CD 206 (M_2) of macrophages; (c) Western blot results of iNOS and CD 206 on day 7; (d) The ratio of iNOS and CD 206 calculated from the Western blots; (e) IL-6, (f) IL-10 and (g) BMP-2 expression from macrophages. The control group was the macrophages cultured on the cell slides. Data presented as mean ± SD, n=3, the error bars indicate the SD, p-values calculated using one-way ANOVA with Sidak's multiple comparison tests, *p < 0.05, **p < 0.01, and ***p < 0.001. NS means no statistical difference (P > 0.05).

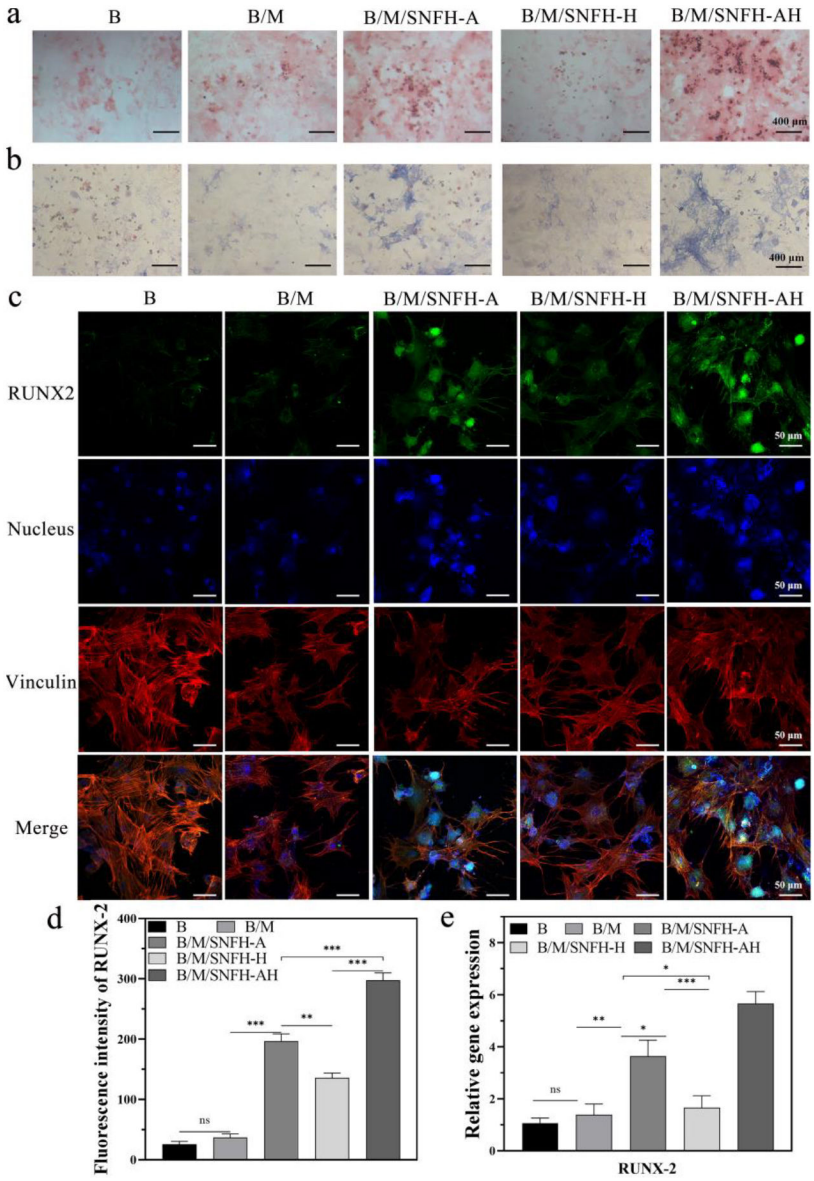

Figure 4.

Effect of immunomodulation by different cryogels on osteogenic differentiation: (a) ARS staining; (b) Alkaline phosphatase staining; (c) immunofluorescence staining of the BMSCs co-cultured with macrophages in different cryogels for 7 days; (d) Fluorescence intensity of RUNX-2 calculated from immunofluorescence staining; (e) The mRNA levels of RUNX-2 of BMSCs. The samples listed as: B, BMSCs were cultured on the cell slides; B/M, BMSCs and macrophages co-cultured on the cell slides; B/M/SNFH-A, B/M/SNFH-H and B/M/SNFH-AH represented BMSCs and macrophages co-cultured with macrophages cultured in SNFH-A, SNFH-H and SNFH-AH, respectively. Data presented as mean ± SD, n=3, the error bars indicate the SD, p-values calculated using one-way ANOVA with Sidak's multiple comparison tests, *$p < 0.05$, **$p < 0.01$, and ***$p < 0.001$. NS means no statistical difference ($P > 0.05$).

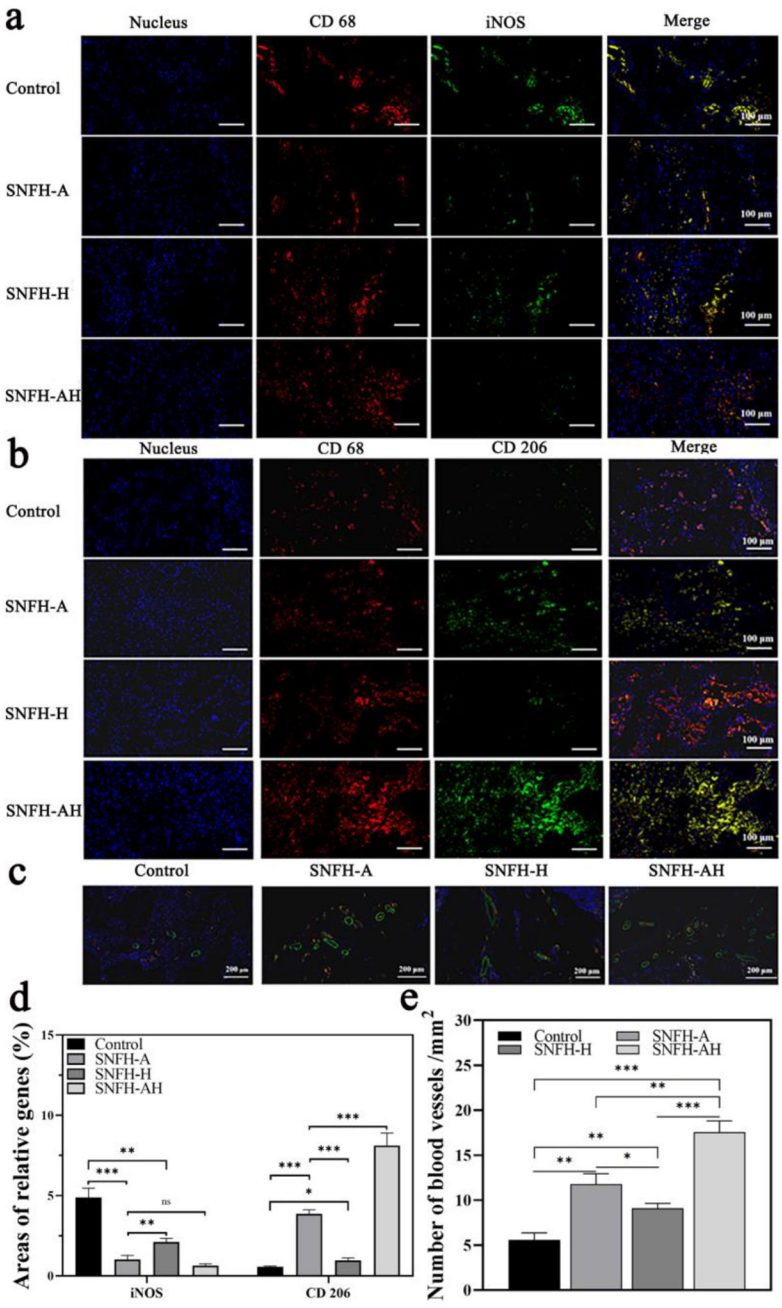

Figure 5.

Immunomodulation and neovascularization in the bone defects: (a) iNOS and (b) CD 206 expression of macrophages; (c) expression of critical factors relative to the process of angiogenesis after cryogel implantation for 2 weeks. CD31 stained red while α-smooth muscle actin positive cells stained green. (d) Quantification of expression of iNOS and CD 206 calculated from images (a, b). (e) Quantification of vessel number calculated from images (c). Density of vessels were calculated by counting the number of vessels in per square millimetre according the immunofluorescent images of CD 31 and α-SMA. Control defects filled with PBS solution. The other groups were filled with the different cryogels.

Data presented as mean ± SD, n=3, the error bars indicate the SD, p-values calculated using one-way ANOVA with Sidak's multiple comparison tests, *p < 0.05, **p < 0.01, and ***p < 0.001. NS means no statistical difference (P > 0.05).

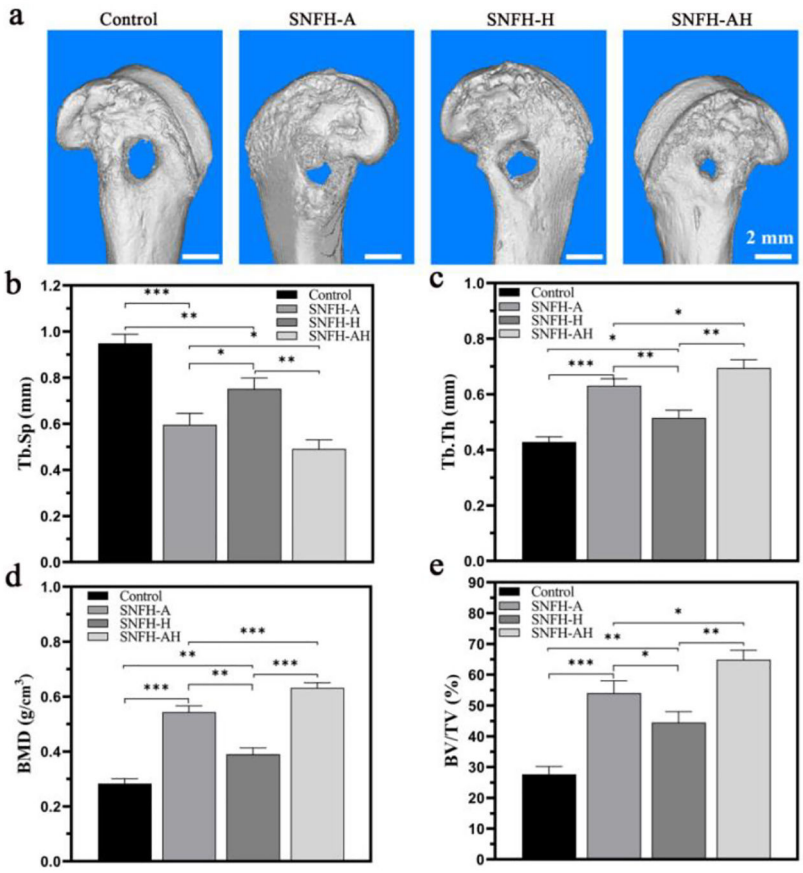

Figure 6.

Micro-CT images and micro-architectural analysis of new bone at defect sites: (a) 3D reconstructed images at 12 weeks after implantation; (b) Trabecular separation (Tb. Sp); (c) Trabecular thickness (Tb. Th); (d) Bone mineral density (BMD); (e) Bone volume/total volume ratio (BV/TV). Control defects filled with PBS solution. The other groups were filled with the different cryogels. Data presented as mean ± SD, n=3, the error bars indicate the SD, p-values calculated using one-way ANOVA with Sidak's multiple comparison tests, *$p < 0.05$, **$p < 0.01$, and ***$p < 0.001$. NS means no statistical difference ($P > 0.05$).

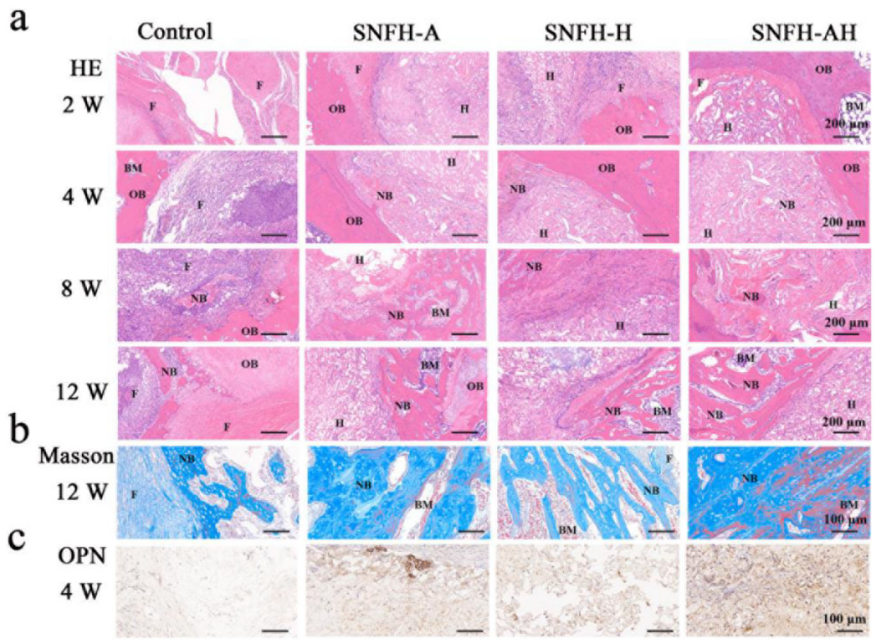

Figure 7.

Quality of regenerated bone in the defects: (a) H&E staining images of defects treated with different cryogels at weeks 2, 4, 8 and 12 after surgery. F indicates fibrotic tissue, H indicates implanted cryogel hydrogels, HB means host bone and NB shows newly formed bone. (b) Masson's trichrome staining of the defects at 12 weeks after surgery; (c) OPN expression in the defects 4 weeks after surgery.

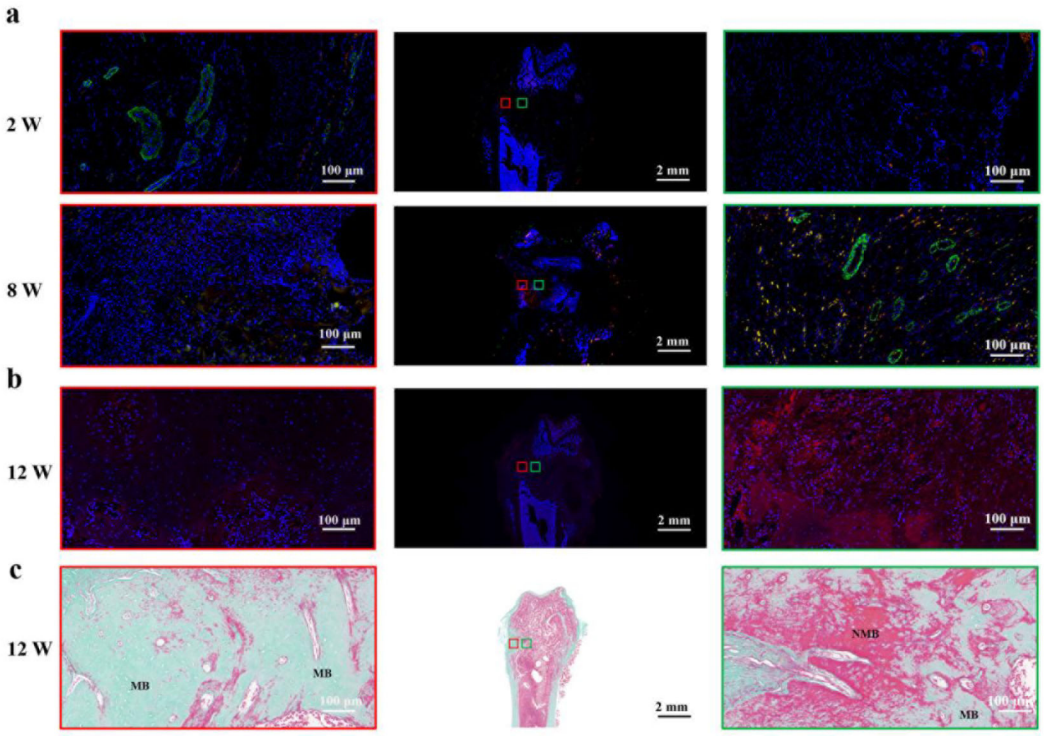

Figure 8.

Influence of anisotropic and homogeneous porous regions on bone regeneration treated with the SNFH-AH cryogels: (a) angiogenesis at the defects after cryogel implantation for 2 and 8 weeks. CD31 stained red while α-smooth muscle actin positive cells stained green. (b) COL-1 expression in the defects treated with the SNFH-AH cryogels. (c) Goldner staining images of defects treated with the SNFH-AH cryogels weeks 12 after surgery. MB means mineralized bone and NMB means non-mineralized bone. The left image was staining results in the anisotropic porous region while the right image was staining results in the homogeneous porous region.

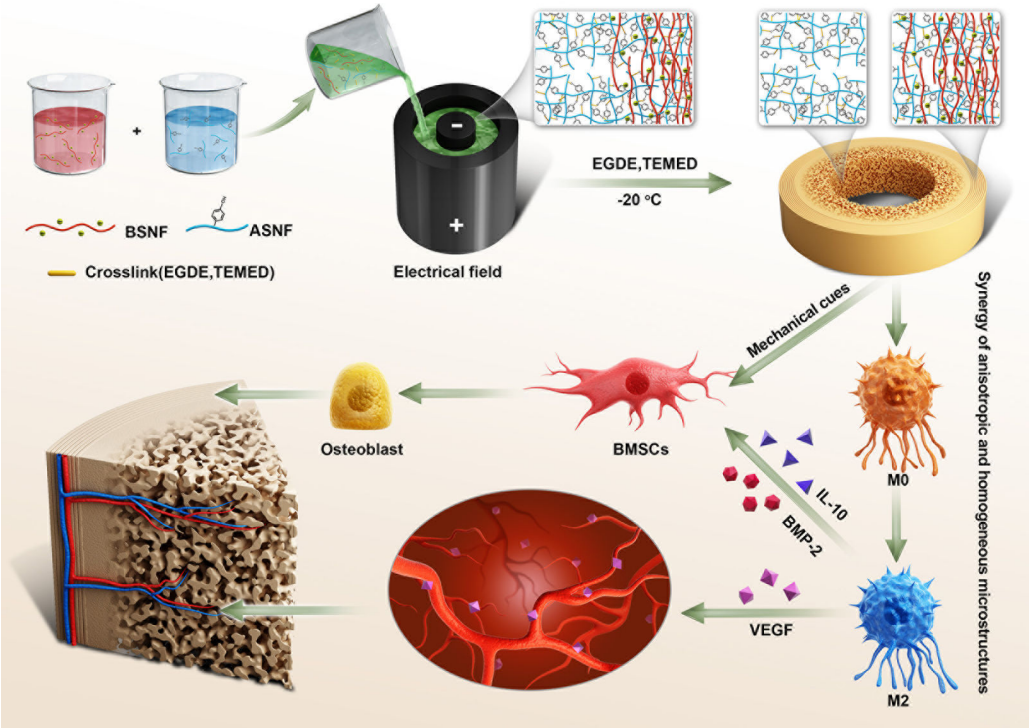

Scheme 1.

Formation of composite cryogels with anisotropic and homogeneous porous structures, which mimic the hierarchical structures of cortical and cancellous bones. The hierarchical structures modulate inflammation, angiogenesis and osteogenesis, optimizing bone regeneration. BSNF, beta-sheet rich silk nanofiber; ASNF, amorphous silk nanofiber.

Table 1.

Sequences of primers used in RT-PCR

Gene	Forward primer sequence (5’ to 3’)	Reverse primer sequence (5’ to 3’)
GAPDH	TGGGTGTGAACCACGAGAA	GGCATGGACTGTGGTCATGA
RUNX-2	CAACCACAGAACCACAAGTGC	AAATGACTCGGTTGGTCTCG
Osteopontin	CCAAGTAAGTCCAACGAAAG	GGTGATGTCCTCGTCTGTA
iNOS	CCTGTGTTCCACCAGGAGAT	CCCTGGCTAGTGCTTCAGAC
CD 206	TCATACCGTGTTGAACCTC	TGGCATTTTACAAATAAATCCTT